THE JOURNAL OF CELL BIOLOGY

Live imaging of apoptosis in a novel transgenic mouse highlights its role in neural tube closure

Yoshifumi Yamaguchi,[1,2] Naomi Shinotsuka,[1] Keiko Nonomura,[1] Kiwamu Takemoto,[3,4] Keisuke Kuida,[5] Hiroki Yosida,[6] and Masayuki Miura[1,2]

[1]Department of Genetics, Graduate School of Pharmaceutical Sciences, The University of Tokyo, Bunkyo-ku, Tokyo 113-0033, Japan
[2]Core Research for Evolutional Science and Technology, Japan Science and Technology Agency, Chiyoda-ku, Tokyo 102-0075, Japan
[3]Graduate School of Medicine, Yokohama City University, Kanazawa-ku, Yokohama 236-0004, Japan
[4]Precursory Research for Embryonic Science and Technology, Japan Science and Technology Agency, Kawaguchi, Saitama 332-0012, Japan
[5]Millennium: The Takeda Oncology Company, Cambridge, MA 02139
[6]Graduate School of Medicine, Saga University, Saga 840-8502, Japan

Many cells die during development, tissue homeostasis, and disease. Dysregulation of apoptosis leads to cranial neural tube closure (NTC) defects like exencephaly, although the mechanism is unclear. Observing cells undergoing apoptosis in a living context could help elucidate their origin, behavior, and influence on surrounding tissues, but few tools are available for this purpose, especially in mammals. In this paper, we used insulator sequences to generate a transgenic mouse that stably expressed a genetically encoded fluorescence resonance energy transfer (FRET)–based fluorescent reporter for caspase activation and performed simultaneous time-lapse imaging of apoptosis and morphogenesis in living embryos. Live FRET imaging with a fast-scanning confocal microscope revealed that cells containing activated caspases showed typical and nontypical apoptotic behavior in a region-specific manner during NTC. Inhibiting caspase activation perturbed and delayed the smooth progression of cranial NTC, which might increase the risk of exencephaly. Our results suggest that caspase-mediated cell removal facilitates NTC completion within a limited developmental window.

Introduction

Many fluorescent reporters that detect the activity of endogenous enzymes and the levels of small molecule messengers have been developed, mainly based on fluorescence resonance energy transfer (FRET) technology. Functional live imaging using these reporters permits cell-signaling activities to be monitored simultaneously with cell behavior in real time; such information should help elucidate the in vivo functions of the signals (Miyawaki, 2003; Kamiyama and Chiba, 2009).

We previously generated a genetically encoded sensor for caspase activation based on FRET, named SCAT3, which contains a substrate sequence recognized by executioner caspases in its linker region between ECFP and Venus (Fig. 1 A; Takemoto et al., 2003). The dissociation of ECFP and Venus upon cleavage of the linker lowers the Venus/ECFP ratio (V/C; the FRET signal) and thereby indicates caspase activation. SCAT3 has been used for the functional live imaging of caspase activation and apoptosis in living *Drosophila melanogaster* (Takemoto et al., 2007; Koto et al., 2009, 2011; Kuranaga et al., 2011; Nakajima et al., 2011). These studies clearly demonstrated the power of live imaging of caspase activation for understanding the dynamics and significance of apoptosis in an in vivo context.

To apply this tool to mammalian living tissues, we first tried to generate SCAT3-expressing transgenic mice by a conventional transgenic approach. We obtained a transgenic mouse line, but they failed to express a sufficient amount of the transgene for detection. This seems true not only for SCAT3 but also for other CFP-YFP–based probes, as few transgenic mice that stably express genetically encoded FRET probes have been reported (Isotani et al., 2004; Tomura et al., 2009). The difficulty in producing such mice may be because of the silencing of transgenes. In this study, we successfully produced transgenic mice that stably express SCAT3 by using an insulator sequence;

Y. Yamaguchi and N. Shinotsuka contributed equally to this paper.

Correspondence to Yoshifumi Yamaguchi: bunbun@mol.f.u-tokyo.ac.jp; or Masayuki Miura: miura@mol.f.u-tokyo.ac.jp

Abbreviations used in this paper: FRET, fluorescence resonance energy transfer; MHNP, midbrain–hindbrain neuropore; NTC, neural tube closure; NTD, neural tube defect; ROI, region of interest.

The Rockefeller University Press $30.00
J. Cell Biol. Vol. 195 No. 6 1047–1060
www.jcb.org/cgi/doi/10.1083/jcb.201104057

Figure 1. **Detection of caspase activation and apoptosis in living embryos of SCAT3 transgenic mice.** (A) SCAT3 transgenic mice. (i) Expression cassette for the SCAT3 transgene. A chicken HS4 insulator (2×) was used to stabilize the transgene expression driven by CAG promoter. (ii) SCAT3 fluorescence (Venus and ECFP) in E9.5 transgenic embryos. (B) Detection of caspase activation and apoptosis in living mouse embryos. Caspase activation is represented as the pseudocolors that correspond to V/C (1.0–0.5). Embryos dissected from the uterus at E8.75 were observed by live imaging for 8 h from the dorsal view (hindbrain). In the otic placode (insets) of cultured embryos, both the appearance of cell debris (i.e., dying cells, circled by white lines in the ECFP images; 4–8 h) and the V/C decline (blue in the V/C images) in those cells were completely suppressed by the genetic ablation of *apaf-1* or a chemical inhibitor of caspases (200 µM zVAD). wt, wild type. (C) Dependence of SCAT3 cleavage on the intrinsic apoptotic pathway in E8.75 embryos analyzed by Western blotting (WB) using an anti-GFP antibody. The two fragments of cleaved SCAT3 (black arrows) were diminished in SCAT3 transgenic embryos (shown as SCAT3 Tg+) cultured with 200 µM zVAD for 6 h or in *apaf-1* (−/−) embryos compared with control littermates (*+/+ or +/−*). The red arrow indicates full-length SCAT3. Molecular mass is indicated in kilodaltons. (D, left) Detection of caspase activation (decline of V/C) in the MHNP ridge. In control *apaf-1*$^{+/-}$ embryos, cells in the MHNP ridge exhibited caspase activation and subsequently became detached (shown by arrowheads). In embryos deficient for *apaf-1* (*apaf-1*$^{-/-}$) or treated with caspase inhibitor (*apaf-1*$^{+/+}$; 200 µM zVAD), detaching cells appeared but showed no sign of caspase activation. (right) Time course of caspase activation during imaging. *I*, intensity. Normalized V/Cs (moving average among three serial time points) are shown by green lines. Bars: (A) 1 mm; (B) 100 µm; (D) 10 µm.

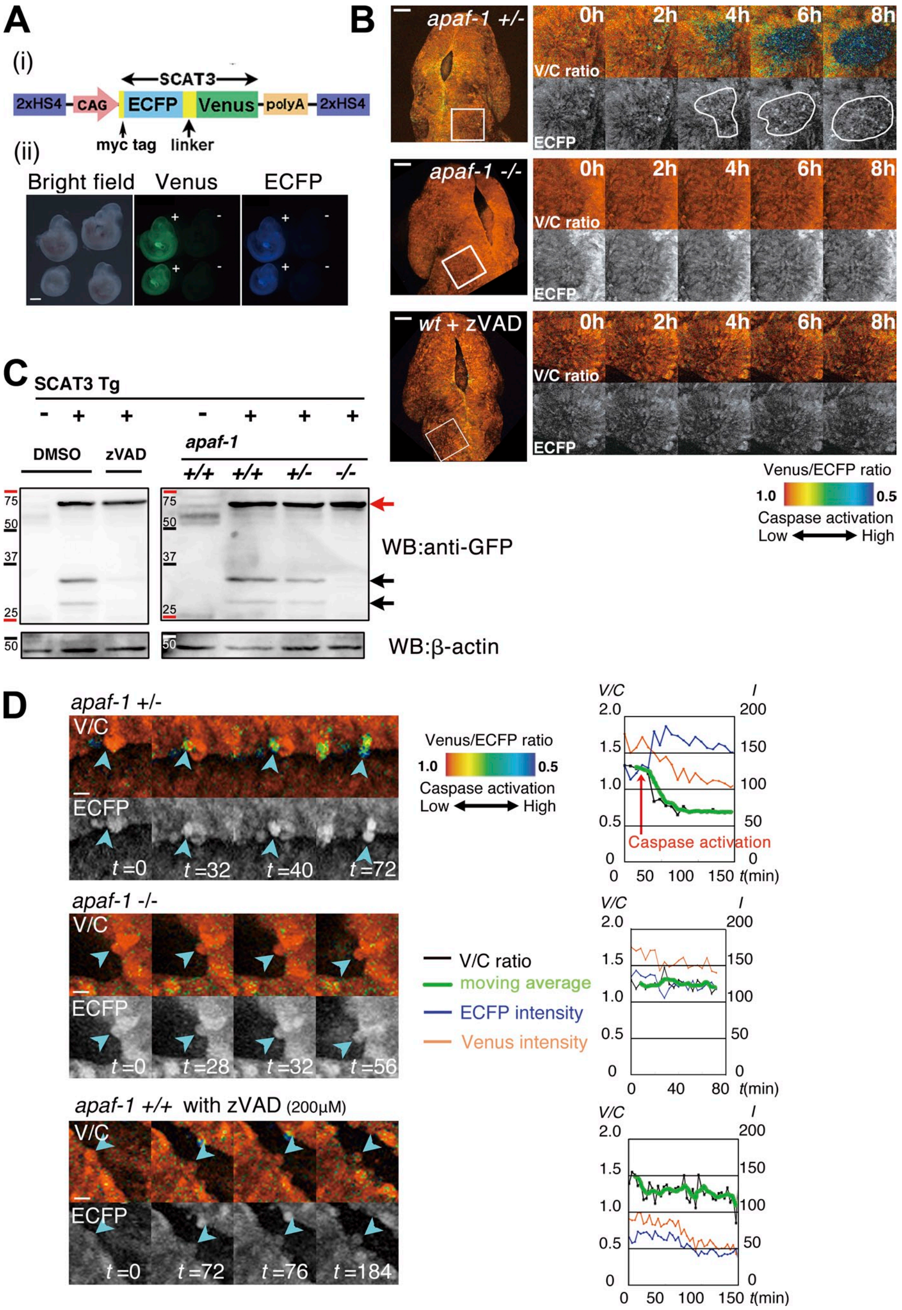

such sequences are able to protect genes from inappropriate signals emanating from their surrounding chromatin environment (Recillas-Targa et al., 2002; West et al., 2002).

Cell death is essential for normal development and for maintaining tissue homeostasis. Among the several types of cell death, which include autophagic cell death and necrosis (Degterev and Yuan, 2008; Yuan and Kroemer, 2010), apoptosis is widely observed in physiological tissue turnover and during development in multicellular organisms (Jacobson et al., 1997). Its mechanism has been the most extensively studied, as caspases, a family of cysteine proteases, were shown to execute cell-killing programs by cleaving specific target proteins (Kumar, 2007). Deficiencies of mitochondrial cell death pathway genes (*caspase-3*, *caspase-9*, or *apaf-1*) in certain genetic backgrounds lead to neurodevelopmental abnormalities such as exencephaly, a phenotype mainly caused by the failure of cranial neural tube closure (NTC; Leonard et al., 2002; Houde et al., 2004).

NTC is the dynamic and complex process that creates the basic morphological scaffold for the central nervous system. Neural tube defects (NTDs), including exencephaly, anencephaly, open spina bifida, and craniorachischisis, are frequently observed in human populations worldwide, and their causes have been intensively studied epidemiologically and experimentally (Copp et al., 2003; Copp and Greene, 2010). Classical embryological manipulation studies showed that coordinated behavior of cells and tissues is required to complete NTC (Schoenwolf and Smith, 1990; Smith and Schoenwolf, 1997). To generate the neural tube from the neural plate, both sides of the plate become raised, forming elevated ridges that bend toward one another until they are apposed, zipped together, and finally fused to form the roof of the neural tube. Massive programmed cell death, mainly apoptosis, occurs during NTC, especially at the neural ridges and midline before and after fusion (Weil et al., 1997; Copp et al., 2003). In addition, chicken embryos treated with pan-caspase inhibitors exhibit NTC failure (Weil et al., 1997). These lines of evidence together suggest that apoptosis is important for the normal completion of NTC. The findings of one study, however, indicate that apoptosis occurs in parallel to neural tube fusion and tissue remodeling in the final steps of NTC because blocking apoptosis acutely during NTC in cultured mouse embryos with a chemical inhibitor of caspases, zVAD-fmk, does not cause any apparent morphological abnormalities like NTDs (Massa et al., 2009). Nevertheless, a deficiency of apoptotic signaling in vivo causes failure of NTC in the cranial region, at the midbrain–hindbrain regions, and, in a few cases, at spinal lumbosacral levels (Honarpour et al., 2001), indicating that dysregulated apoptosis may affect other aspects of NTC than tissue fusion. Thus, it remains unclear how the inhibition of apoptosis affects the cranial NTC and leads to NTDs such as exencephaly.

To clarify the significance and roles of apoptosis during the cranial NTC, the effect of inhibiting apoptosis on the cellular and morphological dynamics of the cranial NTC and on the particular NTC steps must be determined. Given that both the cranial NTC and apoptosis occur too rapidly for conventional fixation methods to determine the relationship between them (Jones et al., 2002; Pyrgaki et al., 2010), a functional live-imaging approach is needed. The SCAT3 transgenic mice we generated here allowed us to perform a real-time detection of caspase activation and apoptotic cells during cranial NTC at both macroscopic and single-cell resolution, which could not have been performed previously. Our live-imaging system revealed the differential behaviors of cells containing activated caspases in a region-specific manner during dynamic morphogenesis and that the absence of these apoptotic cells leads to delayed cranial NTC, thereby possibly increasing the risk of exencephaly. We believe that the real-time detection of cells with activated caspases in living tissue has great potential for providing mechanistic insights into the effects of dying cell behavior in vivo.

Results

Generation of SCAT3 transgenic mice that reveal caspase activation to visualize apoptosis in living embryos

SCAT3 contains a substrate sequence recognized by executioner caspases in its linker region between ECFP and Venus (Fig. 1 A). The dissociation of ECFP and Venus upon cleavage of the linker lowers the FRET signal and the V/C and thereby indicates caspase activation. After several failed attempts to generate SCAT3 transgenic mice, we obtained stable transgene-expressing mouse lines by using cytomegalovirus immediate early enhancer-chicken β-actin hybrid (CAG) promoter with chicken insulator sequences, which can be used to reduce variability in a transgenic mouse founder line by acting as barriers against gene silencing (Fig. 1 A; Niwa et al., 1991; Potts et al., 2000; Recillas-Targa et al., 2002; West et al., 2002; Hsiao et al., 2004; Moriyama et al., 2007).

To examine whether the probe effectively detected caspase activation and apoptosis in living tissue, we first focused on development of the otic placode because it is known that massive apoptosis occurs during otic vesicle formation (Barrow et al., 2000; Cecconi et al., 2004). Embryos dissected from the uterus at embryonic day 8.75 (E8.75) were observed by live imaging for 8 h in culture from the dorsal view (hindbrain; see Materials and methods). In the otic placode (Fig. 1 B, insets), a decreased V/C, indicating caspase activation (green and blue cells in V/C images of *apaf-1*$^{+/-}$ in the top row of Fig. 1 B) and the emergence of cell debris, was observed (i.e., dying cells, circled by white lines in the 4–8 h ECFP images of *apaf-1*$^{+/-}$ in Fig. 1 B; *n* = 5). In contrast, these events were completely suppressed in *apaf-1*$^{-/-}$ embryos (*n* = 3) or wild-type embryos cultured with a pan-caspase inhibitor, zVAD (200 µM; *n* = 3; Fig. 1 B). Western blotting analysis of the embryos indicated that the V/C changes were largely dependent on the cleavage of SCAT3 by caspases (Fig. 1 C). In addition, it was possible to perform time-lapse tracking of an apoptotic cell by V/C at single-cell resolution (Fig. 1 D; see the section after next). Thus, SCAT3 faithfully detected caspase activation and apoptosis at both macroscopic and single-cell resolutions in living mouse embryos.

Visualization of the cranial NTC in the macroscopic scale by a fast-scanning confocal microscope

To visualize NTC in living SCAT3 transgenic mouse embryos, we also set up a live-imaging system with a fast-scanning confocal microscope, which allowed us to scan whole head regions (200–400-µm depth) within a short time (~2 min/embryo) and to reduce photobleaching and phototoxicity as much as possible (Fig. 2 A). In mice and possibly in humans, NTC begins at multiple points along the neural tube with different timing (Fig. 2 B; Copp et al., 2003). During NTC, the neural folds become elevated, bend toward the midline, and fuse together by direct contact of nonneural ectoderm cells from both sides, which we hereafter call boundary cells, to form the neural tube (Fig. 2 C, i–iv; Pyrgaki et al., 2010). Observation of the cranial NTC in living SCAT3 transgenic embryos in our system was consistent with patterns of NTC previously described in fixed embryos (Sakai, 1989; Juriloff et al., 1991; Golden and Chernoff, 1993; Copp et al., 2003); the cervical region of the neural tube was the first to close (closure I; α in Fig. 2 B), and the closure extended rostrocaudally from this site. Rostral closure I initiated the zipping of the boundary cells (Fig. 2 D and Video 1). As the neural tube at rhombomere 5 (r5) and 4 was zipping closed (arrows in Fig. 2, D and E), at r3–r2 and the midbrain, the neural plates began to bend, and the dorsal ridges of the neural plates began to flip (Fig. 2, C [ii and iv] and D [dotted lines]). Closure II was initiated at the forebrain–midbrain boundary (β in Fig. 2 B), and the subsequent zipping spread rostrocaudally. The rostrally directed closure II met closure III to seal the forebrain region, and the caudally directed closure II met rostrally directed closure I to seal the midbrain–hindbrain neuropore (MHNP), thus completing the cranial NTC (Fig. 2 [B and F] and Video 2). Thus, our system allowed us to monitor the entire cranial NTC process in a living embryo.

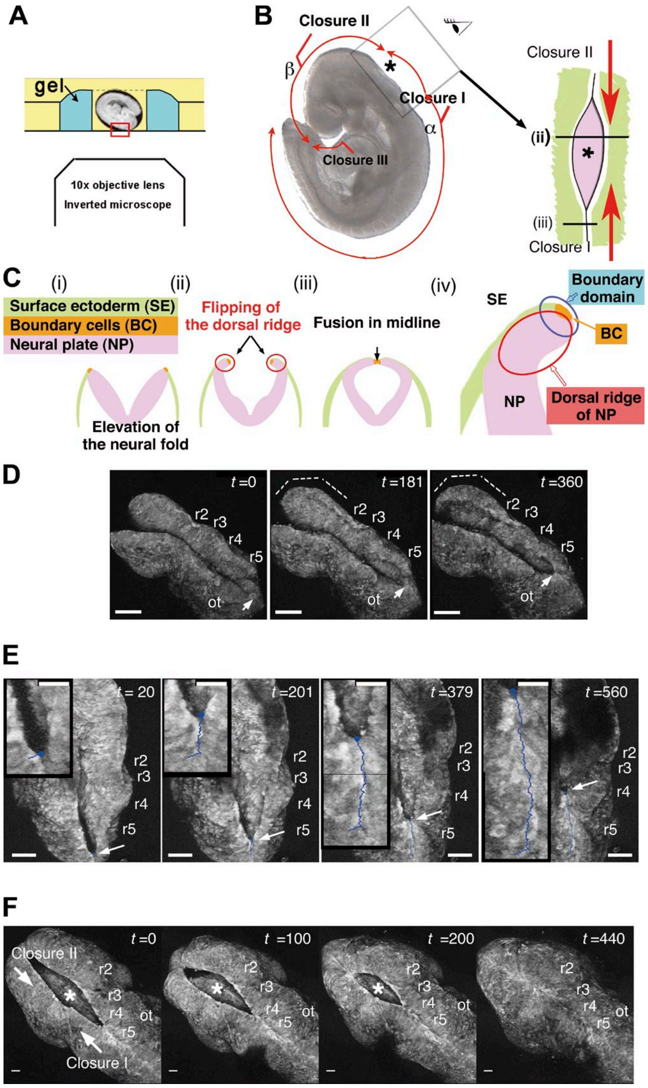

Figure 2. **Time-lapse imaging of the cranial NTC under a fast-scanning confocal microscope.** (A) System for time-lapse imaging of the cranial NTC. Embryos undergoing NTC (somite stage 9–11 for zipping closure I in rhombencephalon and somite stage 12–16 for closures I and II to seal MHNP) were dissected from the uterus and yolk sac and were placed into holes in 2% low temperature–melting agarose on glass-bottom dishes, which were filled with culture medium, and placed in a humidified 37°C/5% CO_2 incubator in order to visualize the hindbrain region (red rectangle). (B, left) Multiple closure sites in the mouse embryo. α and β represent initiation sites of closures I and II, respectively. The MHNP was observed by live imaging (asterisk enclosed by the square). (right) The MHNP (asterisk) is closed by closures I and II. (C) A schematic illustration of the cranial NTC. (i–iii) NTC steps shown as transverse sections along the rostrocaudal axis (indicated in B for ii and iii). (iv) High-magnified view of the dorsal ridge. We termed regions around the boundary cell as the boundary domain (shown by blue circle), including the adjacent surface ectoderm and the edge of the dorsal ridge of the neural plate (red circle). (D) Time-lapse imaging of the cranial closure I in SCAT3 transgenic mice. ot, otic placode. *t*, imaging duration (minutes). Flipping of the neural ridges in the prospective midbrain and hindbrain is emphasized by dotted lines. Bars, 150 µm. (E) Zipped regions were traced (jagged blue line). Bars, 100 µm. (insets) High-magnification views of zipping are shown. Bars, 25 µm. (D and E) Arrows indicate forward zipping edges of closure I. (F) Time-lapse imaging of closures I and II at the MHNP (asterisks) in SCAT3 transgenic mice. Arrows indicate forward zipping edges of closures I and II. Bars, 50 µm.

Differential dynamics of cells containing activated caspases during NTC: Conventional apoptotic cells (C-type) and dancing apoptotic cells (D-type)

To examine the relationship between apoptosis and the progression of the cranial NTC, we first observed the dynamics of apoptosis at single-cell resolution in the prospective midbrain–hindbrain, where rostral closure I and caudal closure II occur, as it was shown that the inhibition of apoptosis results in its malformation (Cecconi et al., 1998; Kuida et al., 1998; Yoshida et al., 1998; Honarpour et al., 2000, 2001). SCAT3 transgenic embryos undergoing closure I at r5–r6 (somite numbers 9–12) were retrieved and observed under our live-imaging conditions. Cells exhibiting a decline of V/C (caspase activation) appeared mainly in the dorsal ridge of the neural plates and in the boundary domain between the neural plates and surface ectoderm (Figs. 1 D and 3 [A–C]). Just after caspase activation ($t = 32$; Fig. 1 D), the cells began to protrude from the epithelial layer, became round, and began to move actively ($t = 40–72$; Figs. 1 D and 3 C [arrows]).

Unexpectedly, these cells rarely fragmented, a hallmark of apoptosis in cultured cells. Instead, they remained continuously attached to and danced around their original sites for a long period ($t = 30–180$; Fig. 3 C [arrows] and Video 3). After that, they tumbled down the neural plate ($t = 180–240$; Fig. 3 C [arrows] and Video 3), and most of them retained their round shape during the imaging period ($t = 330$; Fig. 3 C). Therefore, we termed these cells D-type (dancing type) apoptotic cells (Fig. 3 D). Some D-type cells disappeared suddenly (Fig. 3 C, arrowheads), mainly by flowing away (not depicted) and possibly by collapsing or being engulfed.

We also observed cells during NTC that we termed C-type (conventional type) apoptotic cells (Fig. 3 D), according to the following criteria. After exhibiting caspase activation ($t = 256$; Fig. 3 E [arrows] and Video 4), these cells shrank ($t = 260$; Fig. 3 E) and then fragmented, thereby forming apoptotic bodies ($t = 276$; Fig. 3 E [arrowheads]), which are hallmarks of apoptosis. Immediately afterward, the fragmented apoptotic bodies disappeared, probably engulfed by surrounding cells. C-type cells were observed not only before the completion of closure (Fig. 3 E) but afterward at the midline (Fig. 3 F and Video 5).

Regional preference in C- and D-type apoptotic cells during cranial NTC

As previously mentioned, briefly, there was a regional difference in the distribution of C- and D-type cells during NTC. C-type cells were found near the boundary domain (Fig. 2 C, iv); boundary cells and adjacent surface ectoderm—not only before the completion of closure (Fig. 3 E) but afterward—were found at the midline (Fig. 3 F and Video 5) by live imaging. On the other hand, the D-type cells originated from the boundary domain, but most of them were derived from the dorsal ridge of neural plate and the boundary cells (Figs. 2 C [iv] and 3 [B and C]).

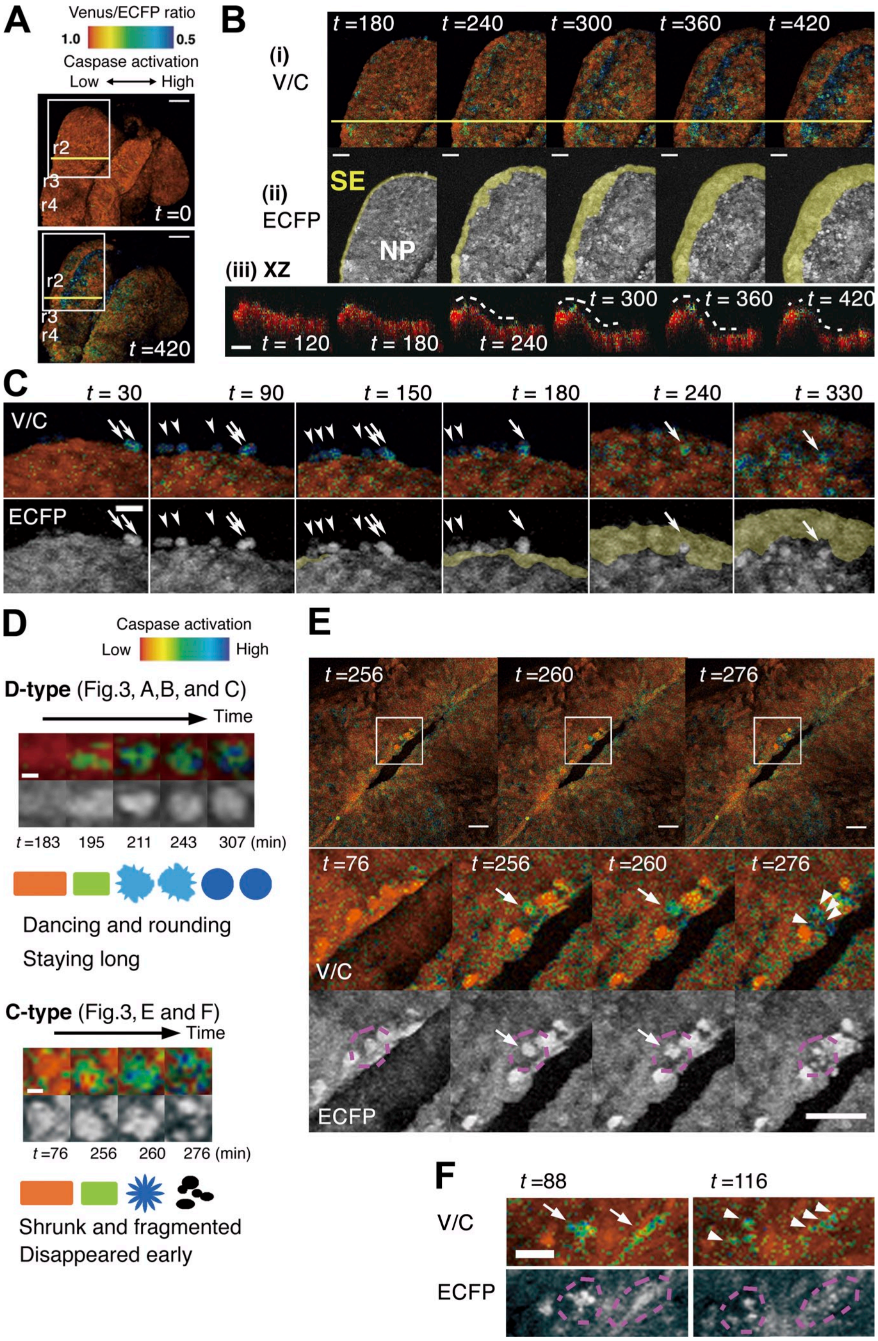

Figure 3. **Real-time detection of apoptotic cells during NTC.** Caspase activation is indicated by the V/C (1.0–0.5). (A–C) Concomitant occurrence of apoptosis and morphological changes in the boundary domain. *t* is indicated in minutes. (B) High-magnification view of insets in A. (i and ii) V/C (i) and ECFP (ii) images. The boundary cells and surface ectoderm (SE) are colored yellow in ii. Concomitant with the flipping of the dorsal ridge of the neural plate (NP), apoptotic cells (blue) appeared beneath the flipping ridges. (iii) Reconstituted transverse (XZ) sections from 4D datasets at r2, indicated by yellow lines in i (also in A). The flipping of the dorsal ridges and bending of the neural plate are indicated by dotted lines. (C) High-magnification views of the flipping dorsal ridge in A and B. Apoptotic cells danced around the dorsal ridge and tumbled down the neural plate (arrows) or disappeared (arrowheads). The flipping edge of the neural plate was being covered by the boundary cells and surface ectoderm, which are colored yellow in the ECFP images (as in B, ii). (D) Features of D- and C-type apoptosis during cranial NTC. (E) A cell showing activated caspase (arrows in V/C images; *t* = 260) shrank (*t* = 260) and became fragmented (*t* = 276; arrowheads) in the boundary domain before the completion of NTC. The same cell is circled by magenta in the ECFP images in the magnified images of the boxed areas. (F) After the MHNP was sealed, extensive caspase activation (arrows) and subsequent cell fragmentation (arrowheads) occurred at the midline. The same cells are circled by magenta in the ECFP images. Bars: (A) 100 µm; (B and E) 50 µm; (C and F) 25 µm; (D) 6 µm.

Interestingly, the D-type apoptotic cells seemed to accumulate in the dorsolateral neural plate as the plate was bending (*t* = 300–420; Fig. 3 B, i and iii).

To confirm that the two types of cells were apoptotic and present in vivo and not an artifact of culture, we observed embryos that were fixed immediately after retrieval and stained with several markers of apoptotic cells. Cells with morphologies similar to the D-type (rounded) and C-type (fragmented) cells were observed by anti–active caspase-3 staining (Figs. 4 [A and B] and S1), suggesting that they were indeed cells with activated caspase in vivo. Furthermore, although the D-type cells retained their cell bodies for a long period after caspase activation, their nucleus was degraded, judging from Hoechst staining and cleaved lamin A staining (Fig. 4, A and C). These results clearly indicated that both the C- and D-type cells were dying by caspase-dependent apoptosis.

To gain insight into the mechanism generating the two different cell types, we examined the expression patterns of various pro- and antiapoptotic proteins by immunostaining during the cranial NTC. We found a regional preference in the activation patterns of the executioner caspases, caspase-3 and caspase-7. Small particles positive for active caspase-3 (about 3–7 µm/diameter), which probably corresponded to fragmented apoptotic bodies derived from the C-type cells, were widely distributed in the boundary domain, the surface ectoderm adjacent to the boundary cells (Fig. 4 D, arrowheads), and the dorsal ridge of neural plates

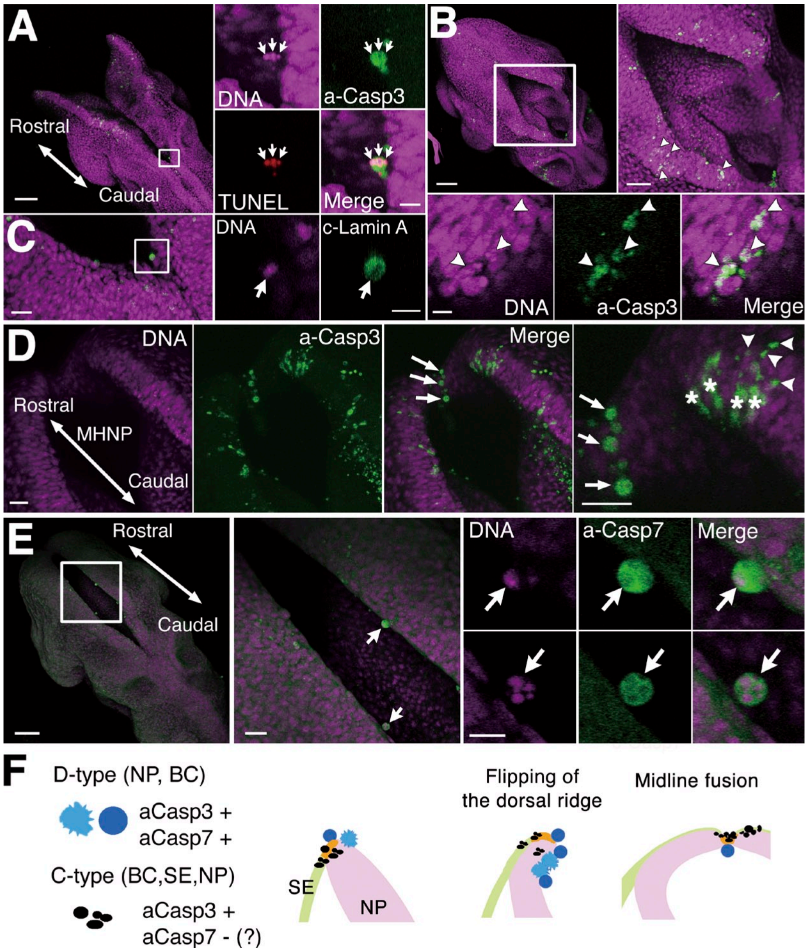

Figure 4. **Regional preferences in caspase activation between C- and D-type apoptotic cells.** Immunostaining of active caspase-3 (a-Casp3) or active caspase-7 (a-Casp7) in embryos undergoing the cranial NTC. Magenta represents Hoechst 33342 staining. (A) In D-type cells, nuclear fragmentation and pyknotic nucleus were observed (magenta; arrows). Bar, 100 µm. (insets) Magnified images of the boxed area are shown. Bar, 10 µm. (B) Active caspase-3 staining, which looked like fragmented apoptotic bodies, was observed in the dorsal ridge of neural plate (green; arrowheads). Bars: (top left) 100 µm; (top right) 50 µm; (bottom left) 10 µm. (C) Signal of cleaved lamin A, which was a substrate of activated caspase, was detected in the D-type cell (green; arrow). Bar, 25 µm. (insets) Magnified images of the boxed area are shown. Bar, 10 µm. (D) Active caspase-3 staining was detected in the surface ectoderm adjacent to the boundary cells (green; arrowheads). It was also observed in rounded D-type cells at the zipping regions (green; arrows) and in the cells aligning the dorsal ridge of the neural plate (green; asterisks). Bars, 25 µm. (E) Active caspase-7 was detected in the D-type cells (green; arrows) detached from the boundary domain. Their nucleus was pyknotic (magenta), indicating that the cells were dying. Bars: (left) 100 µm; (middle) 25 µm; (right) 10 µm. (F) Distribution of two types of apoptotic cells during NTC. The neural plate (NP) is shown in purple, the surface ectoderm (SE) in green, and the boundary cells (BC) between the neural plate and surface ectoderm in orange.

(Fig. 4 B, arrowheads). There were also many cells positive for active caspase-3 that had a neuroepithelial morphology (Fig. 4 D, asterisks) in the dorsal ridge of the neural plate in the midbrain–hindbrain regions. In this case, however, it was difficult to determine which type of apoptosis they were destined to undergo from only the static images. Rounded D-type cells (about 10 µm/diameter) were also positive for active caspase-3 and were located near the zipping point of the closure (arrows in Fig. 4, A and D). There were few signals in the surface ectoderm far from the MHNP around E9.0. On the other hand, active caspase-7 staining was detected in the rounded D-type cells that were detached or already removed from the dorsal ridge of the neural plate (Fig. 4 E, arrows). It was also weakly detected in the cells lining the boundary ridge but rarely in the neural plate (unpublished data). Thus, caspase-3 was activated widely in the dorsal ridge of the neural plate (neuroepithelial cells) and the boundary domain, whereas caspase-7 was activated in the detaching D-type cells (Fig. 4 F).

Kinetic difference in caspase activity between the C- and D-type cells

One of the advantages of SCAT3 is that it enables kinetic measurement of caspase activity by changes of the V/C that is based on the cleavage of SCAT3, thereby revealing the timing of the initial caspase activation and dying process in living tissues. To compare the kinetics of caspase activity quantitatively between the two types of apoptotic cells, we determined the V/C in dying cells over time (see Materials and methods). Interestingly, the C- and D-type cells differed in their kinetics of caspase activity; in all the C-type cells examined (n = 14/14), the V/C rapidly dropped within ~15 min (mean time: 8.0 ± 3.2 min; n = 14), after which the cells underwent cell fragmentation within 10 min (n = 9/14) or, at the most, 20 min (n = 5/14; Fig. 5 A). Thus, the transition from initial caspase activation to cell fragmentation in the C-type cells occurred quickly within ~30 min (t = 256–276; Figs. 3 E and 5 A).

In contrast, D-type cells (n = 9/9) exhibited a slower initial decline in the V/C than C-type cells; this decrease continued for ~30 min (mean time: 16.0 ± 5.6 min; n = 9) and then plateaued (Fig. 5 B). Nevertheless, the cells never underwent cell fragmentation, which was the previously described hallmark of the D-type cells, and persisted for at least ~3 h (Fig. 5 C). Thus, the caspase activity determined by SCAT3 cleavage rose rapidly and severely in the C-type cells but comparatively mildly in the D-type cells (Fig. 5 D). Collectively, by using the SCAT3 transgenic mice, we were able to visualize the dynamics and kinetics of apoptosis and its relationship to morphogenetic movement in living animals during NTC (Fig. 4 F).

Insufficient morphological change in the neural ridge in apoptosis-deficient embryos

To examine how apoptosis contributes to the dynamics of NTC, we next performed live-imaging analyses of embryos deficient for intrinsic apoptotic pathway genes (*apaf-1*$^{-/-}$ or *casp-3*$^{-/-}$;

see Materials and methods; Kuida et al., 1996; Yoshida et al., 1998). In these mutant embryos (somites 10–12), neither D- nor C-type apoptotic cells (Fig. 6, A and B) were observed, and the flipping and bending of the neural plate (Fig. 6 A, arrows) in the presumptive midbrain–hindbrain were severely reduced (compare Fig. 6 [A and B] with Fig. 3 [A and B] and Video 6 with Video 7). Interestingly, the hindbrain dorsal ridges in *apaf-1*$^{-/-}$ embryos exhibited repeated squeezing motions, but they failed to complete the apposition and zipping (Video 6).

Delayed cranial NTC by inhibition of apoptosis both in utero and ex utero

As reduction in bending of the cranial neural folds and in flipping of the dorsal ridges of the neural plates makes contact difficult between the dorsal ridges at the site of closure II (Copp et al., 2003), we assumed that the inhibition of apoptosis might disturb or delay the contact and the subsequent closures. We examined this possibility by precisely assessing the timing and mode of closures in embryos that were immediately fixed after retrieval from the uterus. Indeed, the beginning of closure II, which is evoked by the direct contact of both sides of the dorsal ridge around the forebrain–midbrain boundary, was delayed in apoptosis-deficient embryos (Fig. 7). Furthermore, after that, closures I and II did not progress as much as in controls at the MHNP (Fig. 7), suggesting that reduction in the bending of neural plates and the flipping of dorsal ridges of the neural plates actually occurs in utero and leads to delayed closure in the absence of apoptosis. However, it is difficult to determine the kinetics of NTC from only static samples. To examine this point directly, we again used live-imaging analysis to evaluate the speed of NTC quantitatively. We focused on the MHNP after closure II began (somite 12–14 stages), as the speed of NTC in the MHNP could be calculated by measuring the MHNP length (*L*) at different time points (Fig. 8 A). The speed of closure was almost constant in each individual, but it was significantly reduced in embryos treated with the pan-caspase inhibitor zVAD (Fig. 8, B–D) or deficient for apoptotic machinery (*apaf-1*$^{-/-}$; Fig. 8, B, E, and F). Although zVAD-treated embryos could complete NTC, which is consistent with a previous study (Massa et al., 2009), our live-imaging analysis clearly revealed that blocking the caspases changed its dynamics; the inhibition of caspase activation reduced the closure speed and delayed the zipping during closures I and II (Fig. 9 A).

Possible consequences of delayed cranial NTC

These in utero and ex utero results suggested that a role of apoptosis in cranial NTC is to facilitate its smooth progression so that neural ridge apposition and the zipping processes occur with the appropriate timing to allow these critical steps to be completed (Fig. 9 A). Indeed, there were some apoptosis-deficient embryos in which a reduced speed of closure caused incomplete NTC during the culture period (~12 h; penetrance: $n = 2/8$ embryos in *apaf-1*$^{-/-}$ embryos and $n = 1/2$ in *caspase-3*$^{-/-}$ embryos), similar to the situation in utero in our breeding colony. In one *apaf-1*$^{-/-}$ embryo that had already reached the stage when closure is normally finished (somite 20) at the start of the live-imaging session, the hindbrain region remained open from r4 to r2 throughout the culture period (Fig. S2, A and B). The length of MHNP decreased, as if the rostral and caudal edges had tried to close the MHNP, but the width of the MHNP increased (Fig. S2 B). In other *apaf-1*$^{-/-}$ or *caspase-3*$^{-/-}$ embryos, the progression of closures I and II suddenly stopped, and the MHNP started to reopen along a rupture in the midline (Fig. S2 C). No wild-type or heterozygous embryos exhibited these defects ($n = 0/19$ *apaf-1*$^{+/+}$ or *apaf-1*$^{+/-}$ and $n = 0/4$ *caspase-3*$^{+/+}$ or *caspase-3*$^{+/-}$ embryos).

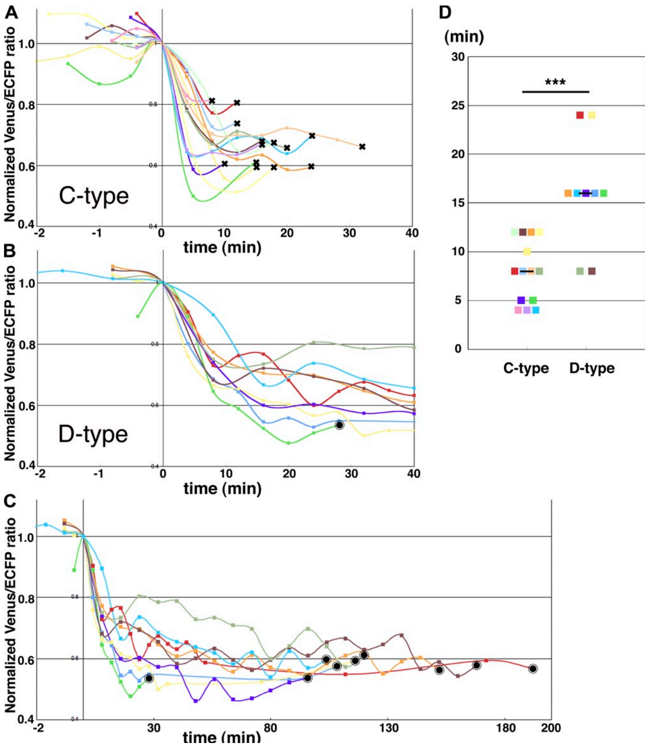

Figure 5. **Difference in the kinetics of caspase activity between the C- and D-type apoptotic cells.** Cell-tracking analysis revealed differential kinetics of caspase activity between the C- and D-type cells. (A–C) Ratio-tracking analysis. Each line corresponds to a single cell. (A) In C-type cells ($n = 14$), the V/C dropped rapidly within 10 min. The x's mark the time when the C-type cell underwent cell fragmentation. (B and C) In D-type cells ($n = 9$), the V/C decreased more slowly than in C-type cells, continuing to decline for an additional ~20 min, and then plateaued. Long-term tracking results are shown in C. The D-type cells did not undergo cell fragmentation during live imaging. The black circle shows the time when the cell could not be tracked anymore as a result of being lost or out of focus. (D) Time to reach the bottom values of V/C. In D-type cells, decline of V/C was significantly slower than in C-type cells. Each square represents individual cells, and its colors correspond to those of A and B. The bottom V/C values of D-type cells were defined as the point at which the V/C reached to the plateau values (see Materials and methods). Black bars indicate mean values (C-type cells: 8.0 ± 3.2 min; D-type cells: 16.0 ± 5.6 min; ***, $P < 0.005$).

Discussion

Cells can undergo multiple forms of cell death (Degterev and Yuan, 2008; Kroemer et al., 2009). Even when apoptosis is prevented, other forms of cell death represented by caspase-independent cell death and necroptosis can still occur (Kroemer et al., 2009). It was recently shown that death by apoptosis is important for the effective clearance of cell debris, which serves

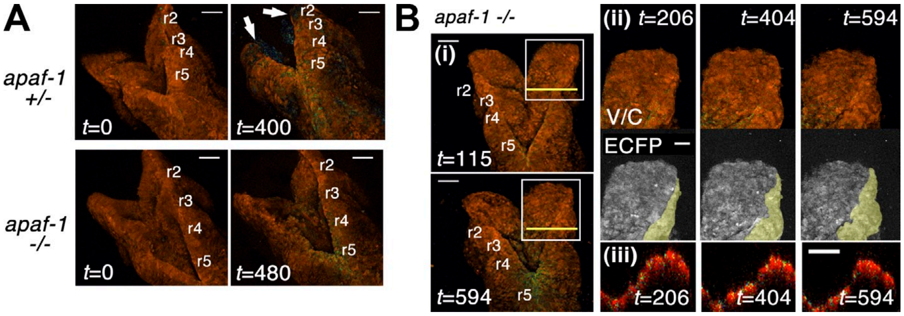

Figure 6. **Insufficient movement of the dorsal ridge of the neural plates by inhibition of apoptosis ex utero.** Comparison of closure I between control (*apaf-1*$^{+/-}$) and apoptosis-deficient (*apaf-1*$^{-/-}$) embryos by live-imaging analysis. Caspase activation is indicated by the V/C (1.0–0.5). (A) Flipping of dorsal ridges (arrows in *apaf-1*$^{+/-}$) was severely reduced in *apaf-1*$^{-/-}$ embryos. Few apoptotic cells (blue cells in *apaf-1*$^{+/-}$) were seen in the *apaf-1*$^{-/-}$ embryos. *t* represents the imaging duration (minutes). (B) Bending of the neural plate was severely reduced in *apaf-1*$^{-/-}$ embryos in prospective midbrain regions. Surface ectoderm is colored yellow in ECFP images in ii (magnified images of the boxed areas on the left). Neither bending nor apoptosis occurred (i and ii). (iii) Reconstituted transverse (XZ) sections from 4D datasets at r2, shown by yellow lines in i. Bars: (A and B [i, and iii]) 100 µm; (B, ii) 50 µm.

to maintain immune tolerance and tissue homeostasis (Elliott and Ravichandran, 2010). However, in most physiological contexts, especially in developmental processes, the mechanism and significance of choosing one form of cell death predominately over another remain to be elucidated (Clarke, 1990). Our live-imaging analysis of apoptosis and morphogenesis using SCAT3 transgenic mice revealed that caspase-activated dying cells with distinct behaviors (C- and D-type) appear in a region-specific manner, suggesting that cells choose the form of apoptosis depending on their lineage or location. Furthermore, we found that inhibiting apoptosis delayed the cranial NTC progression (rostral closure I and caudal closure II), clearly indicating that apoptosis, not other types of cell death, is the critical form of programmed cell death for the cranial NTC.

One study showed that NTC is completed in whole-embryo culture even when apoptosis is acutely prevented by a pan-caspase inhibitor or p53 inhibitors, suggesting that apoptosis is not required for the completion of NTC (Massa et al., 2009). However,

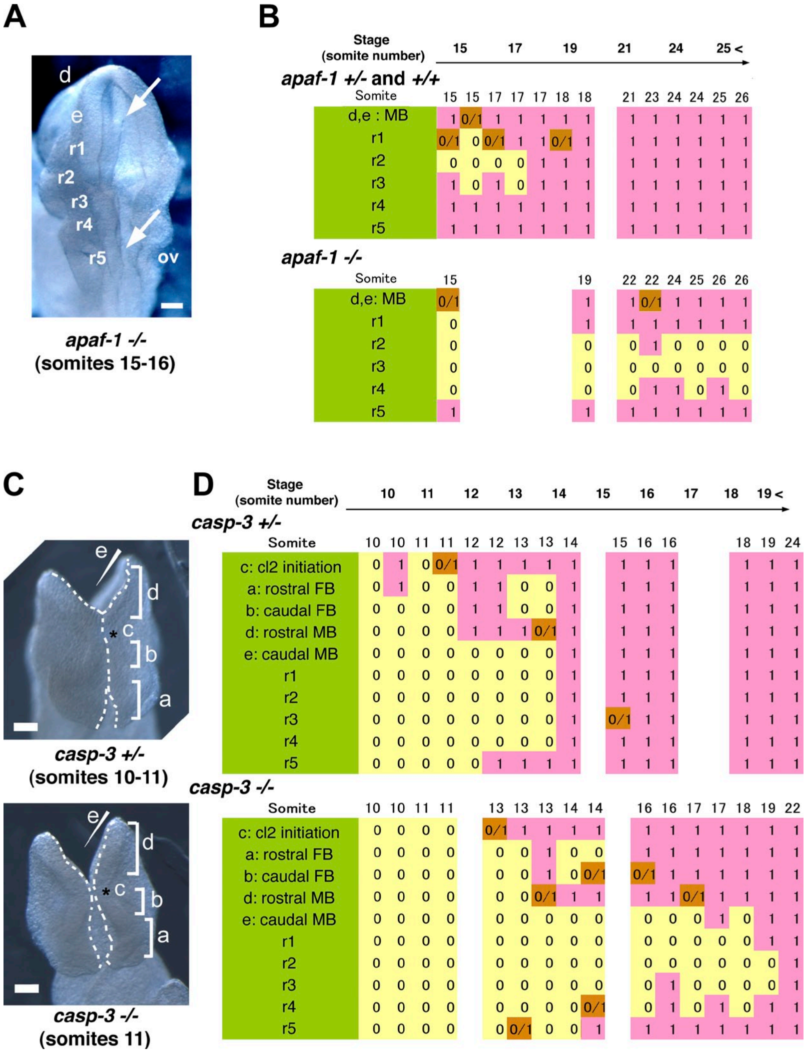

apaf-1 +/- and +/+

Somite	15	15	17	17	17	18	18	21	23	24	24	25	26
d,e : MB	1	0/1	1	1	1	1	1	1	1	1	1	1	1
r1	0/1	0	0/1	1	1	0/1	1	1	1	1	1	1	1
r2	0	0	0	0	1	1	1	1	1	1	1	1	1
r3	1	0	1	0	1	1	1	1	1	1	1	1	1
r4	1	1	1	1	1	1	1	1	1	1	1	1	1
r5	1	1	1	1	1	1	1	1	1	1	1	1	1

apaf-1 -/-

Somite	15	19	22	22	24	25	26	26
d,e: MB	0/1	1	1	0/1	1	1	1	1
r1	0	1	1	1	1	1	1	1
r2	0	0	0	1	0	0	0	0
r3	0	0	0	0	0	0	0	0
r4	0	0	0	1	1	0	1	0
r5	1	1	1	1	1	1	1	1

casp-3 +/-

Somite	10	10	11	11	12	12	13	13	14	15	16	16	18	19	24
c: cl2 initiation	0	1	0	0/1	1	1	1	1	1	1	1	1	1	1	1
a: rostral FB	0	1	0	0	1	1	0	0	1	1	1	1	1	1	1
b: caudal FB	0	0	0	0	1	1	0	0	1	1	1	1	1	1	1
d: rostral MB	0	0	0	0	1	1	1	0/1	1	1	1	1	1	1	1
e: caudal MB	0	0	0	0	0	0	0	0	1	1	1	1	1	1	1
r1	0	0	0	0	0	0	0	0	1	1	1	1	1	1	1
r2	0	0	0	0	0	0	0	0	1	1	1	1	1	1	1
r3	0	0	0	0	0	0	0	0	1	0/1	1	1	1	1	1
r4	0	0	0	0	0	0	0	0	1	1	1	1	1	1	1
r5	0	0	0	0	0	1	1	1	1	1	1	1	1	1	1

casp-3 -/-

Somite	10	10	11	11	13	13	13	14	14	16	16	17	17	18	19	22
c: cl2 initiation	0	0	0	0	0/1	1	1	1	1	1	1	1	1	1	1	1
a: rostral FB	0	0	0	0	0	0	1	0	0	1	1	1	1	1	1	1
b: caudal FB	0	0	0	0	0	0	1	0	0/1	0/1	1	1	1	1	1	1
d: rostral MB	0	0	0	0	0	0	0/1	1	1	1	1	0/1	1	1	1	1
e: caudal MB	0	0	0	0	0	0	0	0	0	0	0	0	1	0	1	1
r1	0	0	0	0	0	0	0	0	0	0	0	0	0	0	1	1
r2	0	0	0	0	0	0	0	0	0	0	0	0	0	0	0	1
r3	0	0	0	0	0	0	0	0	0	0	1	0	0	0	0	1
r4	0	0	0	0	0	0	0	0	0/1	0	1	0	1	0	1	1
r5	0	0	0	0	0	0/1	0	0	1	1	1	1	1	1	1	1

Figure 7. **Delay of closure by inhibition of apoptosis in utero.** Delayed progression of closures I and II at the forebrain and the MHNP of apoptosis-deficient embryos in utero. The degree of delay in the cranial closures I and II in embryos deficient for *apaf-1*$^{-/-}$ (shown in B) or *casp-3*$^{-/-}$ (shown in D) was represented as a score sheet. (A) *apaf-1*$^{-/-}$ embryo exhibiting delayed closures at the MHNP dorsal view (midbrain–hindbrain) of the embryo. Arrows indicate MHNP edges. d, rostral midbrain; e, caudal midbrain; ov, otic vesicle. (B and D) Representation as a score sheet of the degree of cranial closures I and II in embryos deficient for *apaf-1*$^{-/-}$ (B) or *casp-3*$^{-/-}$ (D). Each column corresponds to an individual embryo with its somite number, and rows indicate the extent of closure. A score of 0 (yellow) indicates unattached or open. A score of 1 (pink) indicates attached or closed (fused). A score of 0/1 (orange) indicates attached but not yet fused. d and e, closure II in the midbrain (MB). FB, forebrain. (C) Frontal views of *casp-3*$^{+/-}$ or *casp-3*$^{-/-}$ embryos are shown. Edges of neural plates are traced by white dotted lines. a, rostral forebrain; b, caudal forebrain; c, closure II initiation sites (shown by asterisks); d, rostral midbrain; e, caudal midbrain. (D) Initiation and progression of closure II in controls occur earlier (at around somite 10–12; cl2 initiation rows) than in *casp-3*$^{-/-}$ embryos (at around somite 13). Midline sealing at r2–4 was completed around somite stage 16–17 in normal embryos but delayed in *apaf-1*$^{-/-}$ and *casp-3*$^{-/-}$ embryos. Bars, 100 µm.

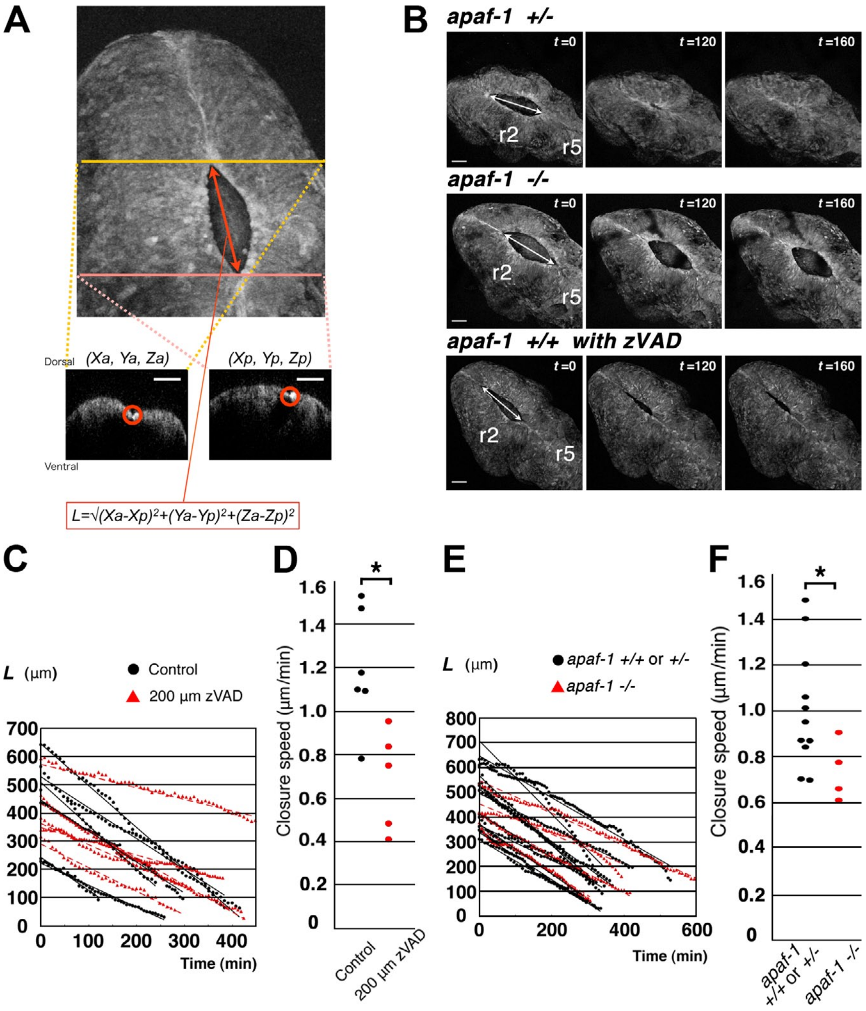

Figure 8. **Delayed closure revealed by quantification of closure speed from live-imaging data.** (A) Measurement of *L* (length of MHNP). Rostral and caudal edges of MHNP were marked in 3D data (red circles), and their coordinate values were used for calculation of *L*. (B) Representative images of MHNP closure in control (*apaf-1*$^{+/+}$ or *apaf-1*$^{+/-}$, *apaf-1*$^{-/-}$, and zVAD-treated embryos). *t* represents the imaging duration (minutes). (A and B) Bars, 100 µm. (C and E) Kinetic analysis of NTC in zVAD-treated embryos (C57BL6×ICR F1 offspring; control, *n* = 6; zVAD treated, *n* = 5; C) or in mutant embryos (C57BL6;129S1 mixed background; *apaf-1*$^{+/+}$ or *apaf-1*$^{+/-}$, *n* = 11; *apaf-1*$^{-/-}$, *n* = 4; E) and length of the MHNP plotted against time. Closure speed was calculated from the linear approximations shown in the graphs (black solid lines and red dashed lines). Note that the closure speed in each embryo was almost constant during the culture period. (D and F) Closure speeds quantified in C and E were significantly slower under caspase-inhibited conditions than under control conditions (*, $P < 0.05$).

it remained unclear whether inhibiting apoptosis causes any changes in NTC dynamics or kinetics and why apoptosis deficiencies in mice cause cranial NTDs in utero. The role of apoptosis and cell death is still confusing in other developmental processes involving tissue fusion or tissue remodeling (for instance, palatogenesis; Iseki, 2011). Observing apoptosis and morphogenesis simultaneously in live animals would provide clues for understanding the contribution of apoptosis to the morphogenesis. Our kinetic analysis by live imaging ex vivo and detailed observation of the cranial NTC in utero did provide a deep understanding of the role of apoptosis during cranial NTC. Although our data support the previous authors' conclusion that apoptosis is not necessarily required for the fusion and completion of cranial NTC, more importantly, our results indicate that apoptosis does contribute to the cranial NTC by facilitating its smooth progression and that incremental effects of delayed closure from the onset of cranial NTC to its end could result in closure failure in the MHNP in utero, where closure I and II finally meet.

A working model for future investigation, consistent with our observations of the MHNP edge dynamics in embryos that failed to finish closure, is that there is a deadline by which the cranial NTC must be completed. This developmental time window hypothesis holds that forces counteracting the closure begin to be generated and surpass those promoting it as embryonic brain development proceeds. By virtue of several factors, including the actomyosin-driven apical constriction that occurs intrinsically in the neural plate (Haigo et al., 2003) and the extrinsic forces provided by the adjacent surface ectoderm that cause the neural plate to bend (Fig. 9 A; Hackett et al., 1997), the cranial NTC is completed before the counteracting forces become elevated, which prevents damage to the neural tube in normal development (Fig. 9 B). However, the cranial NTC fails to close or reopens if there is an inappropriate time lag between the completion of closure and the counteracting force elevation, owing to any genetic, environmental, or physical disturbance that affects cell proliferation, differentiation, adhesion, migration, or cell death.

Hundreds of mouse mutants with NTDs have revealed causal relationships between NTDs and genetic mutations (Copp et al., 2003; Wang et al., 2006; Copp and Greene, 2010). For example, a disturbance in planar cell polarity signaling causes convergence and extension defects that perturb the apposition of the neural ridges, resulting in NTDs in various vertebrate models, including mice (Wallingford and Harland, 2002; Wallingford, 2006). In many other cases, however, the detailed mechanism linking a genetic mutation with the consequent NTD remains to be elucidated. The kinetic analysis of NTC and

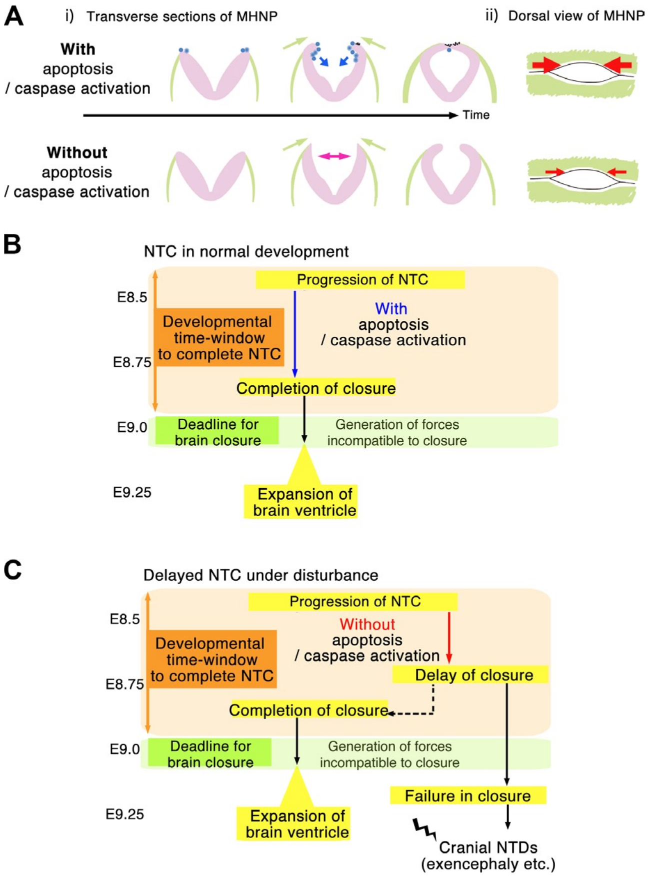

Figure 9. **Developmental time window model for cranial NTDs such as exencephaly.** (A) A schematic representation of NTC in control and apoptosis-deficient embryos. (i and ii) Transverse (i) and dorsal (ii) views of MHNP. The types of apoptotic cells are as shown in Fig. 3 D. Apoptosis helps smooth the morphological changes of the neural plate (blue arrows). Surface ectoderm may provide forces that cause the neural plate to flip and bend (green arrows). As a consequence of the reduced bending in the absence of apoptosis (pink arrows), closure progressed more slowly (shown by small red arrows in ii). The neural plate is shown in purple, and the surface ectoderm is shown in green. (B and C) Developmental time window model for the cranial NTC. (B) NTC must be completed by a developmental deadline (about somite stage 20), when forces incompatible with NTC may arise. Apoptosis helps smooth the progression of NTC, allowing it to be completed by the deadline. (C) Even when closure is delayed, the embryo can develop without NTDs, as long as NTC can be completed before the deadline (case indicated by dotted arrow). However, if closure is not completed by the deadline, cranial NTC ends in failure to close at the MHNP, resulting in cranial NTDs such as exencephaly.

caspase activation by live-imaging analysis at both macroscopic and single-cell resolutions may reveal such links and improve our understanding of NTDs and how to prevent them.

The results of viewing NTC kinetically might also explain the variable phenotypic penetrance of some cranial NTD-causing mutations on different genetic backgrounds (Fleming and Copp, 2000). Because the mode of NTC itself is highly variable among embryos and strains (Juriloff et al., 1991; Golden and Chernoff, 1993; Fleming and Copp, 2000), it is reasonable that the impact of delayed NTC completion could vary among them as well. Indeed, apoptosis-deficient mutants show differential phenotypic penetrance dependent on their genetic background. The penetrance of brain malformation is high in the 129/C57BL6 mixed background but reduced in the C57BL6 background (Leonard et al., 2002; Houde et al., 2004). As we used a 129/C57BL6 mixed background colony in which a few mice homozygous for *apaf-1* or *caspase-3* could survive to adulthood (unpublished data), this phenotypic penetrance could explain why most of the homozygous mutants exhibited slow progression of the NTC but completed it under the live-imaging conditions, except for a few that failed to finish NTC and exhibited exencephalic phenotypes.

The exact mechanisms by which inhibiting apoptosis affects the dynamics of the cranial NTC and reduces the speed of closure in the MHNP remain to be elucidated. In dorsal closure in *Drosophila*, apposing epidermal sheets contact one another and seal with zipperlike dynamics at the midline, and the inhibition or promotion of apoptosis in amnioserosa cells that connect to the lateral epidermis delays or accelerates the dorsal closure process, respectively, suggesting that extrusion of apoptotic cells contribute to dorsal closure by force generation (Toyama et al., 2008). In this regard, the D-type apoptotic cells arising from the neural ridge in mammals could be beneficial for the smooth flipping of the neural ridge. D-type cells were frequently observed close to the zipping point of the MHNP, as if they were being extruded from the neural ridge, raising the possibility that there is a physical force to extrude D-type cells from the neural ridge.

In cultured mammalian cells, apoptotic cells are removed rapidly and can affect the cytoskeleton of neighboring cells, probably providing a mechanism not only for smoothing morphogenesis but also for keeping epithelial integrity (Rosenblatt et al., 2001). It is assumed that apoptotic cells should be extruded from the epithelial tissues without cell fragmentation to maintain epithelial integrity as well as proper morphogenesis. Because the D-type cells are not fragmented and therefore too large to be engulfed by nonprofessional phagocytes like epithelial cells, which possess relatively low phagocytic capacity, they are probably engulfed by professional phagocytes like macrophages and microglias (Parnaik et al., 2000). The D-type apoptotic cells that persist in the lumen in vivo could be finally eliminated by professional phagocytes, as macrophage-like cells appear in the cranial region around E9–10, long after the generation of D-type cells and the completion of NTC (unpublished data). In contrast, the fragmentation of C-type cells into small apoptotic bodies—the conventional form of apoptosis—should allow surrounding nonprofessional epithelial cells to engulf the debris rapidly.

In addition to these physical effects on morphological forces, apoptotic cells can affect their neighbors by releasing signaling molecules (Chera et al., 2009; Li et al., 2010). It would be interesting to examine whether the distinct behaviors and kinetics of caspase activity between the C- and D-type cells (Figs. 3 D and 5) have different effects on their immediate surroundings. The gradual decline of the V/C, representing the mild activity of caspases in the D-type cells, might give them time to cleave sufficient amounts of caspase substrates to secrete/expose "find-me," "eat-me," or other signals like growth-promoting signals before they are eliminated (Grimsley and Ravichandran, 2003). We observed the activation of caspase-7 in D-type cells that were already or not yet detached from the boundary ridge but rarely in the neuroepithelium, where caspase-3 was abundantly activated. The two executioner caspases show redundant but distinct substrate specificities and enzymatic (DEVDase) activity, with caspase-7 having weaker cleaving abilities for some of caspase-3's substrates (Walsh et al., 2008). Consistent with this, the efficiency of SCAT3 cleavage, as measured by in vitro cleavage assay, is different between caspase-3 and -7; a constitutive active form of caspase-3 exhibited higher efficiency in cleaving SCAT3 compared with caspase-7 (Fig. S3), suggesting that slow kinetics of the V/C decline in D-type cells may be attributed to the activation of caspase-7, which is frequently observed in those cells (Fig. 4 E). The activated caspase-7 in D-type cells might compete with caspase-3 for its substrates, reducing the efficiency of substrate cleavage that otherwise enables the rapid execution of apoptotic change. Thus, this difference in substrate cleavage efficiency might also explain the different behaviors between the D-type cells, which activate caspase-7 strongly, and the C-type cells, in which caspase-7 activation was rarely detected.

In conclusion, we successfully established transgenic mice that stably express a FRET-based fluorescent probe by using insulator sequences. The functional live-imaging analysis of caspase activation and NTC in these mice has great potential to reveal the dynamics of NTC in various NTD mutants and to provide mechanistic insights into the causal relationships between gene function or environmental perturbation and NTDs, thereby also improving our understanding of the causes of human NTDs. Likewise, visualizing the kinetics of caspase activation and the behaviors of cells containing activated caspases in vivo using SCAT3 transgenic mice should help elucidate the consequences and significance of caspase activation and apoptosis not only in development but also in tissue homeostasis and diseases.

Materials and methods

Generation of SCAT3 transgenic mice

To express the SCAT3 transgene stably, we used the chicken 2×HS4 insulator (a gift from G. Felsenfeld, National Institutes of Health, Bethesda, MD; Recillas-Targa et al., 2002). The EcoRI fragment of pJC13-1 was removed and replaced by a NotI site, and the BamHI fragment of pJC13-1 was then removed and replaced by the SCAT3 expression cassette (CAG-SCAT3-pA) to create the 2×HS4-CAG-SCAT3-pA-2×HS vector. The vector was digested with NotI and SalI, and the digested fragment was purified with the QIAEX II kit (QIAGEN) and introduced into fertilized C57BL/6 eggs to generate transgenic mice. Founder males were genotyped by PCR and backcrossed to C57BL/6 females. The PCR primers and conditions used for genotyping were as follows: forward 5′-CAGAAGCTGATCTCGGAGGA-3′ and reverse 5′-GCACTGCACGCCCCAGGT-3′ at 94°C for 30 s, 55°C for 30 s, and 72°C ×30 cycles.

Live imaging of NTC

Before the embryos were dissected, all media and dishes were prewarmed to 37°C. Then, 300 µl of 2% low-melting agarose was poured into a glass-bottom dish, and a hole for sinking embryos was made at least 1 h before filling the dish with medium. Pregnant mice were killed at 8.5 d postcoitum by cervical dislocation, and the uterus was removed and placed in Opti-MEM (Invitrogen). Embryos in their yolk sac were removed from the uterus and transferred into Opti-MEM containing 10% FBS. The yolk sac and amnion were then carefully removed while the embryo was kept on a heater, and the embryos were placed in no. 0 glass-bottom dishes (thickness of ∼100 µm; Matsunami Glass Ind., Ltd.) filled with Opti-MEM containing 50% immediately centrifuged rat serum (Charles River) and 0.1% penicillin-streptomycin (Pn/St) or Opti-MEM containing 25% FBS (JRH Biosciences), 25% house-made immediately centrifuged mouse serum (for observing closures in the MHNP), and 0.1% Pn/St. For preparing immediately centrifuged mouse serum, blood was collected and immediately centrifuged, as was the rat serum for whole-embryo culture. Dissected embryos were sunk into the agarose holes and observed with an inverted confocal microscope (TCS SP5; Leica) equipped with a galvo stage and a resonant scanner for fast scanning using an HCX PL FLUOTAR 10× 0.3 NA dry objective (Leica). During imaging, the dishes were kept in a humidified cell culture incubator with a continuous supply of 5% CO_2/air at 37°C (Tokai Hit Company).

ECFP was excited by a 442-nm diode laser (20–40% power), and the emissions of ECFP and Venus (FRET) were simultaneously detected with two detectors by the resonant scanner (8,000 Hz; Leica). The image (512 × 512 pixels) acquisition interval was 4–8 min, and the thickness of the z slices was 4 µm (total of 50–100 slices/each time point), depending on the experiment. For the pharmaceutical inhibition of caspase activity, zVAD-fmk (200 µM final concentration; 1/1,000× dilution of 200 mM stock in DMSO; Merck) was used. We confirmed that the addition of 0.1% DMSO did not have any obvious effect on NTC, which is consistent with a previous study (Massa et al., 2009). Live-imaging experiments were performed using embryos obtained by intercrossing $SCAT3^{tg/tg}$ male mice with Institute of Cancer Research female mice for the zVAD experiments or by intercrossing $SCAT3^{tg/tg}$;$apaf\text{-}1^{+/-}$ male mice with $SCAT3^{tg/+}$;$apaf\text{-}1^{+/-}$ female mice for examining $apaf\text{-}1^{-/-}$ embryos. To observe NTDs occurring in the 129S1×C57BL/6 mixed background by the inhibition of apoptosis, we crossed 129S1 strain mice once with mice heterozygous for *apaf-1* or *caspase-3* knockout alleles that were maintained on the C57BL/6 genetic background. After imaging, genotypes of the embryos were determined by PCR, as previously described (Kuida et al., 1996; Yoshida et al., 1998).

Image processing

The V/C images were generated using MetaMorph (Molecular Devices) or Volocity (PerkinElmer) software. V/C tracking was manually performed in maximum-projected images using Volocity or ImageJ (National Institutes of Health) software. XZ transverse images were also processed from raw 4D datasets with Volocity or ImageJ. For highly magnified images (Fig. 3, C and D), a smooth zoom filter was applied to the V/C and ECFP images using Volocity only for visualization. The video editing and linear adjustment of intensity also only for visualization were performed with ImageJ. To eliminate the XY drift in time-lapse series, the stackreg plug-in was used. The Image, Stack and Timelapse Arrow Labeling Tool was used to add arrows to time-lapse videos.

Tracking and quantification of the V/C in D- and C-type cells

By using V/C images that were projected by maximum intensity projection along the z axis, we manually tracked caspase-activated cells that showed pseudocolor changes from red to blue. Each region of interest (ROI) was set to track a presumable single cell on ECFP or Venus images by using ImageJ's plug-in ROI Manager, and V/C was calculated by ImageJ with the plugin Ratio Profiler. On the ratio graph plotted along time, we defined the time point at which V/C decreases by over 10% of the previous V/C for the first time as the $t = 1$ point and the previous time point as $t = 0$. The V/C at $t = 0$ was V/C_0. The reason why we chose this criteria is that noise in the measurement was estimated to be ∼10% of V/C in the case of C-type cells. To compare the degree of ratio decline among different cells, V/C was normalized by V/C_0. In the case of C-type cells, tracking was finished by cell fragmentation, shown by x's in Fig. 5 A. When cell fragmentation occurs, signals from healthy cells underlying or surrounding the fragmented apoptotic bodies could also be collected, which led to increases in the V/C. That is why the V/C increased in the last points in some of C-type cells and why we have not performed V/C tracking after cell fragmentation. Although this V/C increase is a kind of error in the measurement, we presented it on the graph in Fig. 5 A because the increases could demonstrate that the C-type cells actually underwent cell fragmentation at the last points. In D-type cells, tracking was finished (shown by black circles in Fig. 5, B and C) by disappearance of the cells, which was probably caused by being out of focus, flowing away, collapsing, or being engulfed. To compare the kinetics of caspase activation between C- and D-type cells, we determined the time point that was the lowest value in the case of C-type cells or that was the beginning of plateau value (V/C_p) in the case of D-type cells. The V/C_p was determined from the graph, based on the estimation that measurement error of the V/C as a result of ROI selection or noise of images was up to ∼0.15 during plateau phase.

Quantification of the length and width of the MHNP and the velocity of NTC

Measurements of the MHNP length (*L*) and width (*W*) were taken from 4D datasets using Volocity. The rostral and caudal edges of the MHNP were manually identified in XYZ views and tracked along the time course. *L* was calculated as the distance between the two edges. *W* was calculated in *apaf-1*$^{-/-}$ embryos as follows: the edges of the MHNP were tracked manually in XYZ views at each time point, and the distance between the left and right edges was measured at the widest point at r2. *L* was plotted over time, and linear approximation was applied to determine the velocity of NTC in each individual. The dataset was analyzed using Student's *t* test after analysis of variance.

Whole-mount immunohistochemistry

For whole-mount staining of caspase-3, caspase-7, and cleaved lamin A, Institute of Cancer Research embryos were collected from the uterus at E8.75 in cold PBS and immediately fixed with 4% PFA for 3 h. The embryos were washed three times and blocked with a blocking buffer (20% immuno-block/10% donkey serum/TBST (TBS with 0.1% Triton X-100) for 1 h. After that, the embryos were incubated with anti–active caspase-3 (1/500× dilution), anti–active caspase-7 (1/200×), or anti–cleaved lamin A (1/100×; Cell Signaling Technology) overnight at 4°C with gentle shaking. After eight washes in TBST, they were incubated with an anti–rabbit IgG antibody conjugated with Cy5 (Jackson ImmunoResearch Laboratories, Inc.) overnight at 4°C, washed again, and observed with a confocal microscope (TCS SP5) using HCX PL FLUOTAR 10× 0.3 NA and HCX APO FLUOTAR 10× 0.4 NA dry objectives (Leica). Can Get Signal solution (Toyobo Co., Ltd.) was used for enhancement of active caspase-7 signals. Whole-mount TUNEL staining was performed before immunohistochemistry by using In Situ Cell Death Detection kits (Roche). For simultaneous detection of SCAT3 ratio changes and caspase activation by immunohistochemistry, *SCAT3*$^{tg/+}$ embryos were dissected from the uterus at E8.75 in cold HBSS and immediately fixed with 2% PFA/0.1% glutaraldehyde/PBS for 20 min on ice. The embryos were washed three times in PBS, and their images were captured by confocal microscopy (TCS SP5) using an HCX PL FLUOTAR 10× 0.3 NA dry objective to measure the V/C. After that, the embryos were incubated with an anti–active caspase-3 antibody overnight at 4°C with gentle shaking. After five washes in PBS, they were incubated with an anti–rabbit IgG antibody conjugated with Cy5 (Jackson ImmunoResearch Laboratories, Inc.) overnight at 4°C, washed again, and observed with a confocal microscope (TCS SP5) using an HCX PL FLUOTAR 10× 0.3 NA dry objective.

Western blotting of embryos

Embryos dissected from the uterus at E8.75 were removed from the yolk sac and cultured for 6 h in Opti-MEM containing 25% immediately centrifuged mouse serum, 25% FBS, and 0.1% Pn/St. After that, embryos were immediately frozen in liquid N_2 and stored until use. For the pharmaceutical inhibition of caspase, *SCAT3*$^{tg/+}$ embryos were removed from the yolk sac and cultured with 200 µM zVAD for 6 h in Opti-MEM containing 25% mouse serum, 25% FBS, and 0.1% Pn/St. To detect the cleavage of SCAT3, embryos were lysed with radioimmunoprecipitation assay buffer containing protease inhibitor mix (Roche), and 20 µg of total protein was loaded in each lane. SCAT3 was detected by using anti-GFP antibody (Roche).

In vitro protein synthesis

For in vitro cleavage assay, SCAT3, reverse caspase-3, and reverse caspase-7 proteins were individually synthesized with the TNT Quick Coupled Transcription/Translation System (Promega) using the 1 µg of pcDNA3 construct plasmids (gifts from R. Takahashi, Kyoto University, Kyoto, Japan) as a template, according to the manufacturer's instructions (Srinivasula et al., 1998; Suzuki et al., 2001; Araya et al., 2002; Takemoto et al., 2003).

DEVDase activity measurements and in vitro cleavage assay

Diluted series of synthesized reverse caspase-3 or -7 were used for DEVD–4-methylcoumaryl-7-amide (MCA) assay and in vitro cleavage assay at the same time. Measurements for DEVDase activities of the caspases and in vitro cleavage assay of SCAT3 were performed as previously described (Takemoto et al., 2003; Ohsawa et al., 2009). For DEVDase activity assay, 200 µl of reaction mixture containing 2 µl of diluted reverse caspase-3 or -7 and 10 µM enzyme substrate Ac-DEVD-MCA (Peptide Institute, Inc.) was incubated at 37°C for 30 min. The level of released 7-amino-4-methylcoumarin was measured using a spectrofluorometer (ARVO X3; PerkinElmer) with excitation at 380 nm and emission at 460 nm, and the DEVDase activity was determined. In parallel, in vitro cleavage assay of SCAT3 was conducted as follows: 1 µl of SCAT3 protein was incubated at 37°C with 2 µl of a diluted series of reverse caspase-3 or -7 for different time periods (0, 10, 20, 30, and 60 min) in reaction mixture (20 mM Hepes-KOH, pH 7.5, 10 mM KCl, 1.5 mM $MgCl_2$, 1 mM EDTA, 1 mM EGTA, 1 mM dithiothreitol, 5 µg/ml pepstatin A, and 0.1 mM PMSF). Western blotting analysis with anti-myc antibody (Invitrogen) was performed to detect cleavage of SCAT3. A representative result at the similar DEVDase activity for each caspases is shown in Fig. S3.

Online supplemental material

Fig. S1 shows the colocalization of anti–active caspase-3 staining and the decreased V/C. Fig. S2 describes methods to measure the width of the MHNP and shows that closures in the MHNP failed to be completed in a few apoptosis-deficient embryos under the live-imaging conditions. Fig. S3 shows differential efficiency of SCAT3 cleavage by reverse caspase-3 and -7 in in vitro cleavage assay. Video 1 shows live imaging of the zipping process in rostral closure I (shown in Fig. 2 E). Video 2 shows live imaging of the sealing MHNP by closures I and II (shown in Fig. 2 F). Video 3 shows the concomitant occurrence of D-type apoptotic cells during neural plate morphogenesis (shown in Fig. 3 C). Video 4 shows the occurrence of C-type apoptotic cells before and during the midline fusion (shown in Fig. 3 E). Video 5 shows the occurrence of C-type apoptotic cells after the midline fusion (shown in Fig. 3 F). Video 6 shows comparison of the neural plate morphogenesis between *apaf-1*$^{+/-}$ and *apaf-1*$^{-/-}$ embryos by the live-imaging analysis of SCAT3 (shown in Fig. 6 A). Video 7 shows the inhibition of smooth neural plate morphogenesis in the absence of apoptosis (shown in Fig. 6 B). Online supplemental material is available at http://www.jcb.org/cgi/content/full/jcb.201104057/DC1.

We are grateful to G. Felsenfeld for the gift of the HS4 insulators, R. Takahashi for providing reverse caspase-3/7, Y. Uchiyama (Juntendo University, Tokyo, Japan) for transferring caspase-3 KO mice, and M. Suzuki (Kumamoto University, Kumamoto, Japan) for transgenic mouse production. We thank the University of Tokyo and Leica Microsystems Imaging Center for imaging analysis. We also thank E. Kuranaga (RIKEN Center for Developmental Biology), T. Chihara, H. Mitchell, and all the members of the Miura laboratory for helpful discussions and comments and M. Sasaki and Y. Fujioka for experimental assistance.

This work was supported by grants from the Japanese Ministry of Education, Science, Sports, Culture, and Technology (to M. Miura and Y. Yamaguchi) and by grants from the Astellas Foundation for Research on Metabolic Disorders, The Naito Foundation, The Cell Science Research Foundation, and a RIKEN Bioarchitect Research grant (to M. Miura). N. Shinotsuka and K. Nonomura are research fellows of the Japan Society for the Promotion of Science.

Submitted: 12 April 2011
Accepted: 9 November 2011

References

Araya, R., R. Takahashi, and Y. Nomura. 2002. Yeast two-hybrid screening using constitutive-active caspase-7 as bait in the identification of PA28gamma as an effector caspase substrate. *Cell Death Differ.* 9:322–328. http://dx.doi.org/10.1038/sj.cdd.4400949

Barrow, J.R., H.S. Stadler, and M.R. Capecchi. 2000. Roles of Hoxa1 and Hoxa2 in patterning the early hindbrain of the mouse. *Development*. 127:933–944.

Cecconi, F., G. Alvarez-Bolado, B.I. Meyer, K.A. Roth, and P. Gruss. 1998. Apaf1 (CED-4 homolog) regulates programmed cell death in mammalian development. *Cell*. 94:727–737. http://dx.doi.org/10.1016/S0092-8674(00)81732-8

Cecconi, F., K.A. Roth, O. Dolgov, E. Munarriz, K. Anokhin, P. Gruss, and M. Salminen. 2004. Apaf1-dependent programmed cell death is required for inner ear morphogenesis and growth. *Development*. 131:2125–2135. http://dx.doi.org/10.1242/dev.01082

Chera, S., L. Ghila, K. Dobretz, Y. Wenger, C. Bauer, W. Buzgariu, J.C. Martinou, and B. Galliot. 2009. Apoptotic cells provide an unexpected source of Wnt3 signaling to drive hydra head regeneration. *Dev. Cell*. 17:279–289. http://dx.doi.org/10.1016/j.devcel.2009.07.014

Clarke, P.G. 1990. Developmental cell death: Morphological diversity and multiple mechanisms. *Anat. Embryol. (Berl.)*. 181:195–213. http://dx.doi.org/10.1007/BF00174615

Copp, A.J., and N.D. Greene. 2010. Genetics and development of neural tube defects. *J. Pathol.* 220:217–230.

Copp, A.J., N.D. Greene, and J.N. Murdoch. 2003. The genetic basis of mammalian neurulation. *Nat. Rev. Genet.* 4:784–793. http://dx.doi.org/10.1038/nrg1181

Degterev, A., and J. Yuan. 2008. Expansion and evolution of cell death programmes. *Nat. Rev. Mol. Cell Biol.* 9:378–390. http://dx.doi.org/10.1038/nrm2393

Elliott, M.R., and K.S. Ravichandran. 2010. Clearance of apoptotic cells: Implications in health and disease. *J. Cell Biol.* 189:1059–1070. http://dx.doi.org/10.1083/jcb.201004096

Fleming, A., and A.J. Copp. 2000. A genetic risk factor for mouse neural tube defects: Defining the embryonic basis. *Hum. Mol. Genet.* 9:575–581. http://dx.doi.org/10.1093/hmg/9.4.575

Golden, J.A., and G.F. Chernoff. 1993. Intermittent pattern of neural tube closure in two strains of mice. *Teratology*. 47:73–80. http://dx.doi.org/10.1002/tera.1420470112

Grimsley, C., and K.S. Ravichandran. 2003. Cues for apoptotic cell engulfment: Eat-me, don't eat-me and come-get-me signals. *Trends Cell Biol.* 13:648–656. http://dx.doi.org/10.1016/j.tcb.2003.10.004

Hackett, D.A., J.L. Smith, and G.C. Schoenwolf. 1997. Epidermal ectoderm is required for full elevation and for convergence during bending of the avian neural plate. *Dev. Dyn.* 210:397–406. http://dx.doi.org/10.1002/(SICI)1097-0177(199712)210:4<397::AID-AJA4>3.0.CO;2-B

Haigo, S.L., J.D. Hildebrand, R.M. Harland, and J.B. Wallingford. 2003. Shroom induces apical constriction and is required for hingepoint formation during neural tube closure. *Curr. Biol.* 13:2125–2137. http://dx.doi.org/10.1016/j.cub.2003.11.054

Honarpour, N., C. Du, J.A. Richardson, R.E. Hammer, X. Wang, and J. Herz. 2000. Adult Apaf-1-deficient mice exhibit male infertility. *Dev. Biol.* 218:248–258. http://dx.doi.org/10.1006/dbio.1999.9585

Honarpour, N., S.L. Gilbert, B.T. Lahn, X. Wang, and J. Herz. 2001. Apaf-1 deficiency and neural tube closure defects are found in fog mice. *Proc. Natl. Acad. Sci. USA*. 98:9683–9687. http://dx.doi.org/10.1073/pnas.171283198

Houde, C., K.G. Banks, N. Coulombe, D. Rasper, E. Grimm, S. Roy, E.M. Simpson, and D.W. Nicholson. 2004. Caspase-7 expanded function and intrinsic expression level underlies strain-specific brain phenotype of caspase-3-null mice. *J. Neurosci.* 24:9977–9984. http://dx.doi.org/10.1523/JNEUROSCI.3356-04.2004

Hsiao, Y.C., H.H. Chang, C.Y. Tsai, Y.J. Jong, L.S. Horng, S.F. Lin, and T.F. Tsai. 2004. Coat color-tagged green mouse with EGFP expressed from the RNA polymerase II promoter. *Genesis*. 39:122–129. http://dx.doi.org/10.1002/gene.20038

Iseki, S. 2011. Disintegration of the medial epithelial seam: Is cell death important in palatogenesis? *Dev. Growth Differ.* 53:259–268. http://dx.doi.org/10.1111/j.1440-169X.2010.01245.x

Isotani, E., G. Zhi, K.S. Lau, J. Huang, Y. Mizuno, A. Persechini, R. Geguchadze, K.E. Kamm, and J.T. Stull. 2004. Real-time evaluation of myosin light chain kinase activation in smooth muscle tissues from a transgenic calmodulin-biosensor mouse. *Proc. Natl. Acad. Sci. USA*. 101:6279–6284. http://dx.doi.org/10.1073/pnas.0308742101

Jacobson, M.D., M. Weil, and M.C. Raff. 1997. Programmed cell death in animal development. *Cell*. 88:347–354. http://dx.doi.org/10.1016/S0092-8674(00)81873-5

Jones, E.A., D. Crotty, P.M. Kulesa, C.W. Waters, M.H. Baron, S.E. Fraser, and M.E. Dickinson. 2002. Dynamic in vivo imaging of postimplantation mammalian embryos using whole embryo culture. *Genesis*. 34:228–235. http://dx.doi.org/10.1002/gene.10162

Juriloff, D.M., M.J. Harris, C. Tom, and K.B. MacDonald. 1991. Normal mouse strains differ in the site of initiation of closure of the cranial neural tube. *Teratology*. 44:225–233. http://dx.doi.org/10.1002/tera.1420440211

Kamiyama, D., and A. Chiba. 2009. Endogenous activation patterns of Cdc42 GTPase within *Drosophila* embryos. *Science*. 324:1338–1340. http://dx.doi.org/10.1126/science.1170615

Koto, A., E. Kuranaga, and M. Miura. 2009. Temporal regulation of *Drosophila* IAP1 determines caspase functions in sensory organ development. *J. Cell Biol.* 187:219–231. http://dx.doi.org/10.1083/jcb.200905110

Koto, A., E. Kuranaga, and M. Miura. 2011. Apoptosis ensures spacing pattern formation of *Drosophila* sensory organs. *Curr. Biol.* 21:278–287. http://dx.doi.org/10.1016/j.cub.2011.01.015

Kroemer, G., L. Galluzzi, P. Vandenabeele, J. Abrams, E.S. Alnemri, E.H. Baehrecke, M.V. Blagosklonny, W.S. El-Deiry, P. Golstein, D.R. Green, et al. 2009. Classification of cell death: Recommendations of the Nomenclature Committee on Cell Death 2009. *Cell Death Differ.* 16:3–11. http://dx.doi.org/10.1038/cdd.2008.150

Kuida, K., T.S. Zheng, S. Na, C. Kuan, D. Yang, H. Karasuyama, P. Rakic, and R.A. Flavell. 1996. Decreased apoptosis in the brain and premature lethality in CPP32-deficient mice. *Nature*. 384:368–372. http://dx.doi.org/10.1038/384368a0

Kuida, K., T.F. Haydar, C.Y. Kuan, Y. Gu, C. Taya, H. Karasuyama, M.S. Su, P. Rakic, and R.A. Flavell. 1998. Reduced apoptosis and cytochrome c-mediated caspase activation in mice lacking caspase 9. *Cell*. 94:325–337. http://dx.doi.org/10.1016/S0092-8674(00)81476-2

Kumar, S. 2007. Caspase function in programmed cell death. *Cell Death Differ.* 14:32–43. http://dx.doi.org/10.1038/sj.cdd.4402060

Kuranaga, E., T. Matsunuma, H. Kanuka, K. Takemoto, A. Koto, K. Kimura, and M. Miura. 2011. Apoptosis controls the speed of looping morphogenesis in *Drosophila* male terminalia. *Development*. 138:1493–1499. http://dx.doi.org/10.1242/dev.058958

Leonard, J.R., B.J. Klocke, C. D'Sa, R.A. Flavell, and K.A. Roth. 2002. Strain-dependent neurodevelopmental abnormalities in caspase-3-deficient mice. *J. Neuropathol. Exp. Neurol.* 61:673–677.

Li, F., Q. Huang, J. Chen, Y. Peng, D.R. Roop, J.S. Bedford, and C.Y. Li. 2010. Apoptotic cells activate the "phoenix rising" pathway to promote wound healing and tissue regeneration. *Sci. Signal.* 3:ra13. http://dx.doi.org/10.1126/scisignal.2000634

Massa, V., D. Savery, P. Ybot-Gonzalez, E. Ferraro, A. Rongvaux, F. Cecconi, R. Flavell, N.D. Greene, and A.J. Copp. 2009. Apoptosis is not required for mammalian neural tube closure. *Proc. Natl. Acad. Sci. USA*. 106:8233–8238. http://dx.doi.org/10.1073/pnas.0900333106

Miyawaki, A. 2003. Fluorescence imaging of physiological activity in complex systems using GFP-based probes. *Curr. Opin. Neurobiol.* 13:591–596. http://dx.doi.org/10.1016/j.conb.2003.09.005

Moriyama, A., I. Kii, T. Sunabori, S. Kurihara, I. Takayama, M. Shimazaki, H. Tanabe, M. Oginuma, M. Fukayama, Y. Matsuzaki, et al. 2007. GFP transgenic mice reveal active canonical Wnt signal in neonatal brain and in adult liver and spleen. *Genesis*. 45:90–100. http://dx.doi.org/10.1002/dvg.20268

Nakajima, Y., E. Kuranaga, K. Sugimura, A. Miyawaki, and M. Miura. 2011. Nonautonomous apoptosis is triggered by local cell cycle progression during epithelial replacement in *Drosophila*. *Mol. Cell. Biol.* 31:2499–2512. http://dx.doi.org/10.1128/MCB.01046-10

Niwa, H., K. Yamamura, and J. Miyazaki. 1991. Efficient selection for high-expression transfectants with a novel eukaryotic vector. *Gene*. 108:193–199. http://dx.doi.org/10.1016/0378-1119(91)90434-D

Ohsawa, S., S. Hamada, H. Asou, K. Kuida, Y. Uchiyama, H. Yoshida, and M. Miura. 2009. Caspase-9 activation revealed by semaphorin 7A cleavage is independent of apoptosis in the aged olfactory bulb. *J. Neurosci.* 29:11385–11392. http://dx.doi.org/10.1523/JNEUROSCI.4780-08.2009

Parnaik, R., M.C. Raff, and J. Scholes. 2000. Differences between the clearance of apoptotic cells by professional and non-professional phagocytes. *Curr. Biol.* 10:857–860. http://dx.doi.org/10.1016/S0960-9822(00)00598-4

Potts, W., D. Tucker, H. Wood, and C. Martin. 2000. Chicken beta-globin 5'HS4 insulators function to reduce variability in transgenic founder mice. *Biochem. Biophys. Res. Commun.* 273:1015–1018. http://dx.doi.org/10.1006/bbrc.2000.3013

Pyrgaki, C., P. Trainor, A.K. Hadjantonakis, and L. Niswander. 2010. Dynamic imaging of mammalian neural tube closure. *Dev. Biol.* 344:941–947. http://dx.doi.org/10.1016/j.ydbio.2010.06.010

Recillas-Targa, F., M.J. Pikaart, B. Burgess-Beusse, A.C. Bell, M.D. Litt, A.G. West, M. Gaszner, and G. Felsenfeld. 2002. Position-effect protection and enhancer blocking by the chicken beta-globin insulator are separable activities. *Proc. Natl. Acad. Sci. USA*. 99:6883–6888. http://dx.doi.org/10.1073/pnas.102179399

Rosenblatt, J., M.C. Raff, and L.P. Cramer. 2001. An epithelial cell destined for apoptosis signals its neighbors to extrude it by an actin- and myosin-dependent mechanism. *Curr. Biol.* 11:1847–1857. http://dx.doi.org/10.1016/S0960-9822(01)00587-5

Sakai, Y. 1989. Neurulation in the mouse: Manner and timing of neural tube closure. *Anat. Rec.* 223:194–203. http://dx.doi.org/10.1002/ar.1092230212

Schoenwolf, G.C., and J.L. Smith. 1990. Mechanisms of neurulation: Traditional viewpoint and recent advances. *Development*. 109:243–270.

Smith, J.L., and G.C. Schoenwolf. 1997. Neurulation: Coming to closure. *Trends Neurosci.* 20:510–517. http://dx.doi.org/10.1016/S0166-2236(97)01121-1

Srinivasula, S.M., M. Ahmad, M. MacFarlane, Z. Luo, Z. Huang, T. Fernandes-Alnemri, and E.S. Alnemri. 1998. Generation of constitutively active recombinant caspases-3 and -6 by rearrangement of their subunits. *J. Biol. Chem.* 273:10107–10111. http://dx.doi.org/10.1074/jbc.273.17.10107

Suzuki, Y., Y. Nakabayashi, K. Nakata, J.C. Reed, and R. Takahashi. 2001. X-linked inhibitor of apoptosis protein (XIAP) inhibits caspase-3 and -7 in distinct modes. *J. Biol. Chem.* 276:27058–27063. http://dx.doi.org/10.1074/jbc.M102415200

Takemoto, K., T. Nagai, A. Miyawaki, and M. Miura. 2003. Spatio-temporal activation of caspase revealed by indicator that is insensitive to environmental effects. *J. Cell Biol.* 160:235–243. http://dx.doi.org/10.1083/jcb.200207111

Takemoto, K., E. Kuranaga, A. Tonoki, T. Nagai, A. Miyawaki, and M. Miura. 2007. Local initiation of caspase activation in *Drosophila* salivary gland programmed cell death in vivo. *Proc. Natl. Acad. Sci. USA*. 104:13367–13372. http://dx.doi.org/10.1073/pnas.0702733104

Tomura, M., Y.S. Mori, R. Watanabe, M. Tanaka, A. Miyawaki, and O. Kanagawa. 2009. Time-lapse observation of cellular function with fluorescent probe reveals novel CTL-target cell interactions. *Int. Immunol.* 21:1145–1150. http://dx.doi.org/10.1093/intimm/dxp080

Toyama, Y., X.G. Peralta, A.R. Wells, D.P. Kiehart, and G.S. Edwards. 2008. Apoptotic force and tissue dynamics during *Drosophila* embryogenesis. *Science*. 321:1683–1686. http://dx.doi.org/10.1126/science.1157052

Wallingford, J.B. 2006. Planar cell polarity, ciliogenesis and neural tube defects. *Hum. Mol. Genet.* 15(Spec No 2):R227–R234. http://dx.doi.org/10.1093/hmg/ddl216

Wallingford, J.B., and R.M. Harland. 2002. Neural tube closure requires Dishevelled-dependent convergent extension of the midline. *Development*. 129:5815–5825. http://dx.doi.org/10.1242/dev.00123

Walsh, J.G., S.P. Cullen, C. Sheridan, A.U. Lüthi, C. Gerner, and S.J. Martin. 2008. Executioner caspase-3 and caspase-7 are functionally distinct proteases. *Proc. Natl. Acad. Sci. USA*. 105:12815–12819. http://dx.doi.org/10.1073/pnas.0707715105

Wang, J., N.S. Hamblet, S. Mark, M.E. Dickinson, B.C. Brinkman, N. Segil, S.E. Fraser, P. Chen, J.B. Wallingford, and A. Wynshaw-Boris. 2006. Dishevelled genes mediate a conserved mammalian PCP pathway to regulate convergent extension during neurulation. *Development*. 133:1767–1778. http://dx.doi.org/10.1242/dev.02347

Weil, M., M.D. Jacobson, and M.C. Raff. 1997. Is programmed cell death required for neural tube closure? *Curr. Biol.* 7:281–284. http://dx.doi.org/10.1016/S0960-9822(06)00125-4

West, A.G., M. Gaszner, and G. Felsenfeld. 2002. Insulators: Many functions, many mechanisms. *Genes Dev.* 16:271–288. http://dx.doi.org/10.1101/gad.954702

Yoshida, H., Y.Y. Kong, R. Yoshida, A.J. Elia, A. Hakem, R. Hakem, J.M. Penninger, and T.W. Mak. 1998. Apaf1 is required for mitochondrial pathways of apoptosis and brain development. *Cell*. 94:739–750. http://dx.doi.org/10.1016/S0092-8674(00)81733-X

Yuan, J., and G. Kroemer. 2010. Alternative cell death mechanisms in development and beyond. *Genes Dev.* 24:2592–2602. http://dx.doi.org/10.1101/gad.1984410